PCCP

ROYAL SOCIETY OF CHEMISTRY

PAPER

View Article Online
View Journal | View Issue

Cite this: *Phys. Chem. Chem. Phys.*, 2020, **22**, 28459

More than protection: the function of TiO_2 interlayers in hematite functionalized Si photoanodes†

Anurag Kawde, [abcd] Alagappan Annamalai,[e] Anita Sellstedt,[f] Jens Uhlig,[d] Thomas Wågberg,[e] Pieter Glatzel*[b] and Johannes Messinger *[ag]

Received 12th August 2020,
Accepted 22nd November 2020

DOI: 10.1039/d0cp04280c

rsc.li/pccp

Worldwide significant efforts are ongoing to develop devices that store solar energy as fuels. In one such approach, solar energy is absorbed by semiconductors and utilized directly by catalysts at their surfaces to split water into H_2 and O_2. To protect the semiconductors in these photo-electrochemical cells (PEC) from corrosion, frequently thin TiO_2 interlayers are applied. Employing a well-performing photoanode comprised of 1-D n-Si microwires (MWs) covered with a mesoporous (mp) TiO_2 interlayer fabricated by solution processing and functionalized with α-Fe_2O_3 nanorods, we studied here the function of this TiO_2 interlayer by high-energy resolution fluorescence detected X-ray absorption near edge structure (HERFD-XANES) spectroscopy, along with X-ray emission spectroscopy (XES) and standard characterization techniques. Our data reveal that the TiO_2 interlayer not only protects the n-Si MW surface from corrosion, but that it also acts as a template for the hydrothermal growth of α-Fe_2O_3 nanorods and improves the photocatalytic efficiency. We show that the latter effect correlates with the presence of stable oxygen vacancies at the interface between mp-TiO_2 and α-Fe_2O_3, which act as electron traps and thereby substantially reduce the charge recombination rate at the hematite surface.

Introduction

Solar-driven photo-electrochemical (PEC) water splitting is one of the most promising routes for producing green fuels, such as hydrogen.[1,2] Efficient PEC devices frequently employ co-catalyst decorated semiconductor photo-electrodes to harvest solar energy and to split water into hydrogen and oxygen. In the search for the most efficient photoelectrode for PEC applications, semiconductors like TiO_2,[3,4] α-Fe_2O_3,[5–7] p/n Si,[8–10] WO_3,[11] CuO_2,[12,13] $BiVO_4$[14–17] and Ta_3N_5[18,19] have been studied since Fujishima and Honda[4] first demonstrated the approach in 1972.

To address potential scalability requirements of the PEC water splitting system, photo-electrodes comprising earth-abundant elements are frequently studied. Manufacturing the components employing solution-based techniques may contribute to further lower the costs of the production process. Examples for earth abundant components employed are silicon (Si) and hematite (α-Fe_2O_3), which under one sun illumination have theoretical solar conversion efficiencies of ~43% and ~15%, respectively.[20,21] However, the stability of Si in the aqueous condition is low,[22] and thus protective layers of, for instance, Ti,[23] Ni,[24] NiO_x,[25] or TiO_2[8,22,26,27] have been applied. The thickness of the most frequently used TiO_2 layers varies from ~2 to 130 nm.[28] It was initially believed that thick TiO_2 films might act as insulators. However, comprehensive studies by the groups of Lewis,[27,28] Tilly,[29,30] and Chorkendorff[31,32] demonstrate that even TiO_2 layers exceeding 100 nm thickness efficiently transfer charges.[29] Interestingly, our recent study of variously functionalized p-Si microwires photoelectrodes indicates that their performance in seawater splitting was even enhanced by a ~50 nm thick mesoporous TiO_2 interlayer.[8] Apparently, the role of the TiO_2 protective layer seems to be more versatile and sophisticated then previously assumed. So far, the role of the TiO_2 protective layer has been primarily studied by photo-electrochemical techniques,[33,34] such as Mott–Schottky measurements[35] and incident photon-to-current efficiency measurements (IPCE),[36] which both give an integral view of the TiO_2 layer. However, there is still

[a] *Umeå University, Faculty of Science and Technology, Department of Chemistry, Sweden*
[b] *European Synchrotron Radiation Facility, Grenoble, France. E-mail: pieter.glatzel@esrf.fr*
[c] *Lund Institute of advanced Neutron and X-Ray Science, Lund University, Sweden*
[d] *NanoLund and Chemical Physics, Department of Chemistry, Lund University, Sweden*
[e] *Umeå University, Faculty of Science and Technology, Department of Physics, Sweden*
[f] *Umeå University, Faculty of Science and Technology, Department of Plant Physiology, Umeå Plant Science Centre (UPSC), Umeå, Sweden*
[g] *Molecular Biomimetics, Department of Chemistry – Ångström Laboratory, Uppsala University, Sweden. E-mail: johannes.messinger@kemi.uu.se*

† Electronic supplementary information (ESI) available. See DOI: 10.1039/d0cp04280c

a lack of understanding from a fundamental atomic level electronic structure perspective.

Using an all solution-based approach, we prepared an n-Si MWs/mp-TiO_2/α-Fe_2O_3 photoanode with highly competitive photo-electrochemical performance and employed it to understand the multiple roles of the TiO_2 interlayer. Our findings suggest that the TiO_2 interlayer not only stabilizes the photoanode, but that the mesoporous (mp) morphology of TiO_2 also acts as a template for the uniform and high surface area hydrothermal growth of the α-Fe_2O_3 co-catalyst. Furthermore, the presence of the mp-TiO_2 interlayer helps to suppress the exciton charge recombination between n-Si MWs photoelectrodes and co-catalysts, which results in better charge transfer kinetics at the electrode/electrolyte interface for water oxidation. High-energy resolution fluorescence detected X-ray absorption near edge structure (HERFD-XANES), and valence-to-core X-ray emission spectroscopy (vtc-XES) at the Ti K-edge demonstrate significant electronic structural changes. At the same time, the Fe K-edge shows little change indicating that the Fe electronic structure is hardly affected by mesoporous TiO_2. Our data suggest that the modification of the electronic structure in the TiO_2 interlayer leads to the exceptional photo-electrochemical performance of our functionalized n-Si photoanode during water oxidation.

Results and discussion

Preparation, morphology, and elemental characterization of functionalized n-Si MWs

A 1-D microwire structure (n-Si MWs) on the surface of a planar n-Si was obtained by treating small pieces of n-Si wafers (2×2 cm^2) with an etching electrolyte comprised of HF and $AgNO_3$ following a previously published procedure (see ESI,† for further details).[37] The resulting n-Si MWs were then spin-coated with a TiO_2 sol–gel,[8,38,39] resulting in n-Si MWs/mp-TiO_2 photoelectrodes. In this process, the block-co-polymer formed spherical micelles that supported the formation of a mesoporous structure of the protective TiO_2 layer (Fig. SI 1, ESI†). The cross-sectional SEM image in Fig. 1a shows that the MW's have a length of about 25 μm and that the TiO_2 coating was complete, yet thin enough not to remove the spacing between the MW. A magnified view of the TiO_2 coating is presented in Fig. 1b. Onto this mesoporous TiO_2 surface, hematite nanorods were hydrothermally grown[40] (see ESI† for further details). The morphology of the resulting n-Si MWs/mp-TiO_2/α-Fe_2O_3 is shown in Fig. 1c and d. It can be seen that despite the acidic conditions during the hydrothermal treatment, the MWs remained mostly intact and that a uniform coverage with *ca.* 200 nm long Fe_2O_3 nanorods were obtained. The excellent coverage of the MW with small, similarly sized α-Fe_2O_3 nanorods suggests that the mesopores of mp-TiO_2 acted as templates for nanorod formation by serving as nucleation sites (see also below). After the synthesis, the samples were annealed at 380 °C, so that the Fe_2O_3 nanorods were converted majorly to alpha hematite (α-Fe_2O_3), as confirmed by X-ray photoelectron spectroscopy (see details in Fig. SI 2, ESI†) and HERFD-XANES (Fig. SI 8 and 9, ESI†). The UV-vis absorption spectrum for bare α-Fe_2O_3 nanorods is presented in Fig. SI 6 c, ESI†).

Fig. 1e shows that in the absence of the TiO_2 layer, the n-Si MWs were partially dissolved by the acidic iron precursor and that about 5 times larger α-Fe_2O_3 rods (*ca.* 1 μm) were obtained that lacked good contact to the n-Si MWs. The increased size of α-Fe_2O_3 nanorod/crystallites is likely due to the significantly fewer nucleation sites provided by n-Si MWs as compared to n-Si MWs/mp-TiO_2.

To test if the surface morphology of the TiO_2 interlayer is indeed essential for an even growth of α-Fe_2O_3 nanorods, we also prepared a photoanode covered by an amorphous TiO_2 layer (n-Si MWs/a-TiO_2/Fe_2O_3). For this, a commercial titanium diisopropoxide bis(acetylacetonate) solution (diluted with ethanol) was applied using a similar spin-coating cycle as for making mp-TiO_2.[6,8] Due to the absence of a block co-polymer like pluronic P123, which is known to promote mesopore formation,[38,39] and due to the lower viscosity of the commercial precursor solution, the resulting TiO_2 film on the n-Si MWs was amorphous (a-TiO_2) and less-even compared to the sol–gel approach. The electron microscopic image in Fig. 1f shows that although the a-TiO_2 interlayer largely protected the n-Si MW during the hydrothermal treatment, fewer Fe_2O_3 crystallites formed on its surface. In addition, the Fe_2O_3 crystallites were of varying size and shape, with less good contact to the a-TiO_2 surface as compared to mp-TiO_2 (Fig. 1d). These results further confirm that mp-TiO_2 acts, *via* its mesopores, as a template for an even and dense hydrothermal growth of well-connected Fe_2O_3 nanorods on top of the MWs. This is important for providing a large catalytic surface and for minimizing the charge carrier transport pathways within Fe_2O_3.[41,42]

Based on this structural inspection, we confirmed that mesoporous TiO_2 protects n-Si MWs in acidic media,[27,43] and propose that it also provides essential nucleation sites for the growth of uniform and well-connected Fe_2O_3 nanorods.

Photo-electrochemical characterization

The PEC performance of the n-Si MWs/mp-TiO_2/α-Fe_2O_3 photoanode was systematically compared to various control samples, such as bare planar n-Si, bare n-Si MWs, n-Si MWs/mp-TiO_2, n-Si MWs/α-Fe_2O_3 and n-Si MWs/a-TiO_2/α-Fe_2O_3. The photocurrent densities (J_{ph}) obtained in aqueous 1 M NaOH electrolyte at one sun illumination and an applied potential of 1.23 V_{RHE} (using a Pt counter electrode) are shown in Fig. 2 (see ESI† for further details). The corresponding *I*/*V* curves are displayed in Fig. SI 3 and SI 4 (ESI†). Fig. 2 shows that for bare planar n-Si the J_{ph} was 0.5 mA cm^{-2}, and that J_{ph} increased to 0.8 mA cm^{-2} for bare n-Si MWs, reflecting the expected improved light absorption and charge-transfer capabilities of the microwire morphology.[8] Interestingly, mp-TiO_2 sol–gel coating of the n-Si MWs led to a further increase of J_{ph} to 1.01 mA cm^{-2}. Most importantly, we noted a significant rise in J_{ph} to 4 mA cm^{-2} ($\pm$0.02 mA cm^{-2}) when the n-Si MWs/mp-TiO_2 were additionally decorated with α-Fe_2O_3 nanorods. In the absence of the protective TiO_2 layer, the photocurrent dropped to 1.2 mA cm^{-2} for n-Si MWs/α-Fe_2O_3, while the n-Si MW/a-TiO_2/α-Fe_2O_3

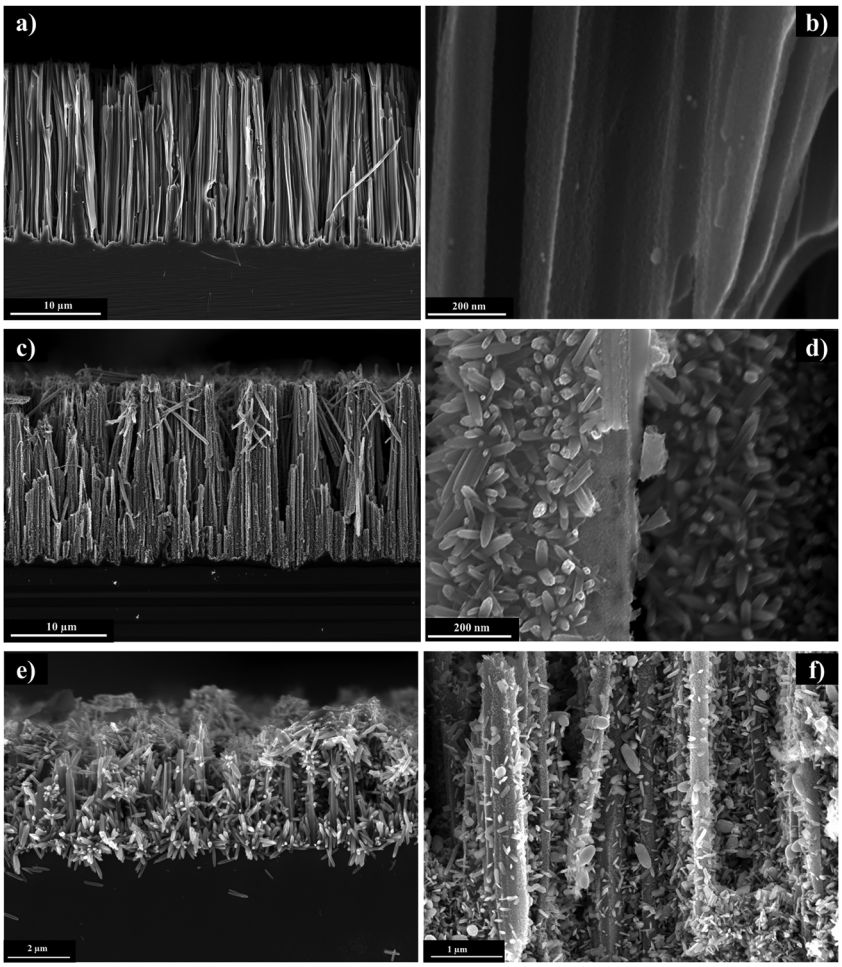

Fig. 1 Cross-sectional SEM images of (a and b) n-Si MWs/mp-TiO_2, (c and d) n-Si MWs/mp-TiO_2/α-Fe_2O_3, (e) n-Si MWs/α-Fe_2O_3 and (f) n-Si MWs/a-TiO_2/α-Fe_2O_3.

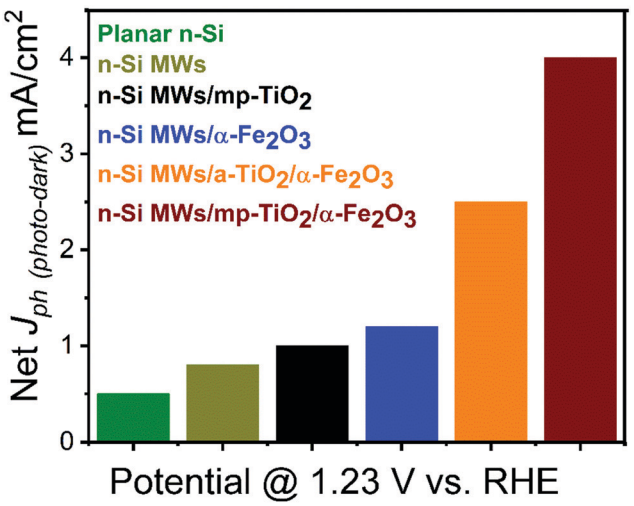

Fig. 2 Net photocurrent responses for bare and functionalized n-Si photoelectrodes at 1.23 V_{RHE}.

photoanode reached a photocurrent of 2.5 mA cm^{-2}, still clearly below the values achieved with a mp-TiO_2 protection layer.

To confirm solar-assisted water splitting, the photogenerated gases were analyzed by sampling the headspace with gas chromatography during a chronoamperometry (at 1.23 V_{RHE}; Fig. SI 5, ESI†). After a short onset period, a nearly stable photocurrent of about 4 mA cm^{-2} was observed for the n-Si MW/mp-TiO_2/α-Fe_2O_3 photoanode over the entire sampling period of 2 hours. The accumulated amounts of photogenerated hydrogen and oxygen collected from the headspace of the PEC cell were 4.33 and 2.2 mmol cm^{-2} (Fig. SI 5b, ESI†), corresponding to faradaic efficiencies of 94% and 97%, respectively.

The TiO_2 interlayer also significantly lowered the onset potential, which we defined here as the potential at which the net photocurrent density reached 0.1 mA cm^{-2}. The value for n-Si MW/mp-TiO_2/α-Fe_2O_3 was only 0.27 V_{RHE} (Fig. SI 3b, ESI†), which is, to the best of our knowledge, the lowest reported onset potential for an undoped α-Fe_2O_3 nanorod based photoanode. In the absence of the mp-TiO_2 interlayer, the onset potential was 540 mV higher (0.81 V_{RHE}; Fig. SI 3b, ESI†). The onset potential for an electrode comprising similar α-Fe_2O_3 nanorods grown on FTO substrate with an a-TiO_2 interlayer was found to be 0.77 V_{RHE}.[6,44] The above experiments indicate that the low onset potential and high J_{ph} reported here may come from having a dual absorber PEC system made of uniformly

sized Fe_2O_3 nanorods that are well connected to the n-Si MWs *via* mp-TiO_2.

To test if the bandgaps of both Si and Fe_2O_3 contribute to the light absorption and thus J_{ph} of the n-Si MW/mp-TiO_2/α-Fe_2O_3 photoelectrode, this multilayer system was selectively excited at either 455 nm, to probe the contribution of the α-Fe_2O_3 nanorods, or at 625 nm for testing the performance if only the n-Si MWs absorbed light (Fig. SI 6, ESI†). Employing 455 nm illumination at 100 mW cm^{-2}, we found that at 1.23 V_{RHE} J_{ph} was 2.4 mA cm^{-2}, which was almost 60% of the photocurrent obtained at 1 sun illumination (Fig. SI 6, ESI†). This indicates that under these experimental conditions the α-Fe_2O_3 nanorods were not simply dark OER catalyst, but instead acted as photo absorbers, while n-Si MWs functioned mainly as a conductive substrate. However, we cannot exclude the possibility that some photons were absorbed also by Si at 455 nm.[45] Importantly, essentially no dark currents were observed for the n-Si MWs/mp-TiO_2/α-Fe_2O_3 photoanode up to at least a potential of 2.5 V_{RHE} (Fig. SI 3c, ESI†). Next, we illuminated our photoanode at 625 nm (100 mW cm^{-2}) to selectively excite Si. At 1.23 V_{RHE} J_{ph} was found to be 3.7 mA cm^{-2} (Fig. SI 6a and b, ESI†), which is 93% of the photocurrent obtained with 1 sun illumination (4.0 mA cm^{-2}).

The capacity of the n-Si MWs/mp-TiO_2/α-Fe_2O_3 photoanode to act as a dual solar absorber system became more apparent when the same experiment was repeated at 2.5 V_{RHE}. Here, the J_{ph} reached 20 mA cm^{-2} under 1 sun illumination. The photocurrent was 20% lower if only the n-Si MWs were excited, and nearly 40% lower if predominantly the α-Fe_2O_3 nanorods were excited (Fig. SI 6, ESI†). We thus conclude that our n-Si MWs/mp-TiO_2/α-Fe_2O_3 photoanode acts as dual absorber system, which is in line with a recent study on another hematite/Si nanowire PEC system.[45] This is schematically illustrated in Fig. 3.

For comparison, Xiaopeng Qi *et al.*[46] reported an n-Si/α-Fe_2O_3 core–shell structure with 25 μm long Si MWs with a J_{ph} of 5.28 mA cm^{-2} at 1.23 V_{RHE} and an onset potential of 0.5 V_{RHE} recorded with a scan rate of 50 mV s^{-1}. For the scan rate of 20 mV s^{-1} used in this study, Xiaopeng Qi *et al.*[46] reported a J_{ph} of ~3.8 mA cm^{-2} at 1.23 V_{RHE} with an onset potential of 0.5 V_{RHE}, which is almost twice the onset potential reported in this study. Recently, Zhongyuan Zhou *et al.*[47] achieved a maximal J_{ph} of 3.12 mA cm^{-2} at 1.23 V_{RHE} and an onset potential of 0.15 V_{RHE} for a Sn-doped hematite film grown on Si MWs, whereas their pristine n-Si/α-Fe_2O_3 photoanode had an onset potential of 0.85 V_{RHE}.

Insight into the mechanism by which TiO_2 improves the performance of photoanodes can be gained by studying the transient photo-response of α-Fe_2O_3 functionalized n-Si MWs without (Fig. 4a and b) and with (Fig. 4c and d) the mp-TiO_2 interlayer. The transient photocurrent density at 1.5 V_{RHE} (2-electrode set-up) was nearly three-fold higher for n-Si MW/mp-TiO_2/α-Fe_2O_3 (6 mV cm^{-2}) than for n-Si MW/α-Fe_2O_3 (2.2 mV cm^{-2}), which is fully consistent with the data in Fig. 2. The sharp spikes visible for both samples in the anodic (positive-spike) and cathodic (negative-spike) regions arise due to the light-induced generation and the dissipation of charge

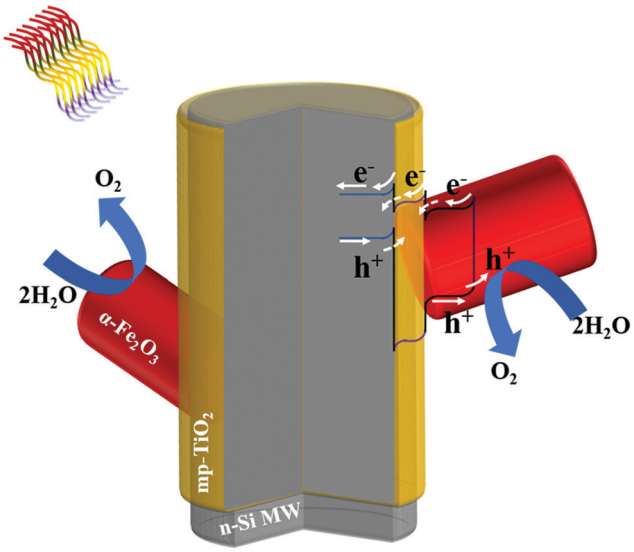

Fig. 3 A schematic representation of energy diagrams and charge-carrier mobility in the n-Si MW/mp-TiO_2/α-Fe_2O_3 photoelectrode.

carriers at the electrode/electrolyte interface. When zooming into the regions of the anodic spikes, it is seen that nearly twice as many charges dissipated in the device lacking the mp-TiO_2 layer, and that this process occurred over a significantly longer time period (Fig. 4b and d). Thus, the presence of a mp-TiO_2 interlayer appears to block the mobility of the holes photogenerated in α-Fe_2O_3 towards the n-Si MWs, since the valence band of mp-TiO_2 lies at lower energy than in α-Fe_2O_3 (Fig. 5b). Assuming the same exciton generation with and without the TiO_2 layer (as the thin TiO_2 layer is optically transparent), the addition of the wide bandgap TiO_2 interlayer thus reduced unproductive charge recombination and thereby allowed

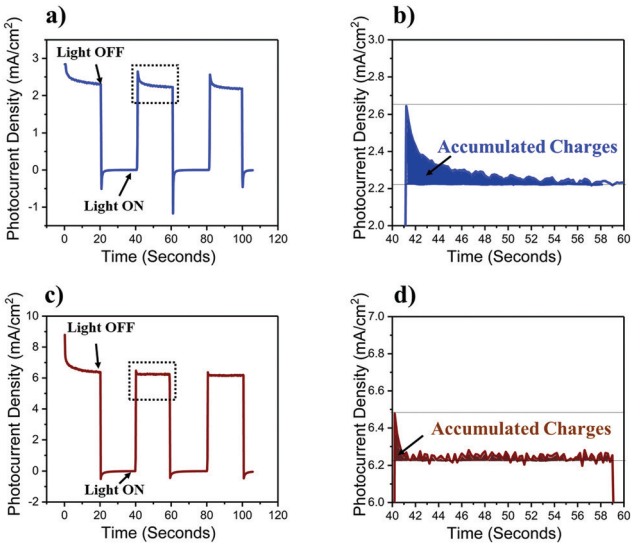

Fig. 4 Transient photocurrent response recorded at 1.5 V_{RHE}. (a) n-Si MW/α-Fe_2O_3 and (b) n-Si MW/mp-TiO_2/α-Fe_2O_3. (c and d) Magnified views of representative anodic spikes.

utilizing the photogenerated holes more efficiently for water oxidation.

In summary, besides the well-known function of the TiO_2 protection layer in passivating the surface defects on Si MWs,[8,32,33] we tentatively assign the superior performance of n-Si MW/mp-TiO_2/α-Fe_2O_3 as compared to n-Si MW/α-Fe_2O_3 to a better interfacial connection between mp-TiO_2 and α-Fe_2O_3, the creation of stable oxygen vacancies (electron traps) in the mp-TiO_2 interlayer, and to the low band edge positioning of TiO_2 that likely suppresses the hole mobility from α-Fe_2O_3 towards n-Si.[32]

Oxygen vacancies

Various studies discussed the role of surface oxygen vacancies in Fe/TiO_2 nanoparticles.[48–51] They establish that oxygen vacancies are generated by high-temperature annealing (~400 °C) of TiO_2 in oxygen-deficient atmospheres. This process can be described using the Kröger–Vink notations:[51–53]

$$O_O^X \overset{TiO_2}{\longleftrightarrow} V_O^{\bullet\bullet} + \frac{1}{2}O_2(g) + 2e' \quad (1)$$

Eqn (1) is a reversible reaction, meaning that the surface oxygen vacancies ($V_O^{\bullet\bullet}$) disappear gradually in ambient conditions (in the presence of molecular oxygen). Early studies from Grätzel and co-workers,[49,54] and Hoffmann and co-workers[50] suggested stabilization of surface oxygen vacancies in the nanoparticulate TiO_2 lattice by the introduction of acceptor type dopants such as Fe^{3+} as ionic charge-compensating species represented by eqn (2):

$$Fe_2O_3 \xrightarrow{TiO_2} 2Fe'_{Ti} + 3O_O^X + V_O^{\bullet\bullet} \quad (2)$$

Previous studies have already correlated the presence of oxygen vacancies in TiO_2 with enhanced photocatalytic properties of TiO_2.[48,52] Additionally, increasing the active surface area of TiO_2 particles by reducing their size has also been employed for enhancing photocatalytic properties of TiO_2.[55,56] As mp-TiO_2 thin films are known for having an about 800 times larger effective surface area than planar TiO_2 thin films,[48,57,58] the incorporation of Fe ions onto mp-TiO_2 thin films may prove to be an effective strategy for stabilizing oxygen vacancies, and to thereby enhance photocatalytic water oxidation efficiency. In our study, the Fe ions were incorporated onto the surface layers of mp-TiO_2 during the hydrothermal growth of α-Fe_2O_3 nanorods onto the surface of mp-TiO_2 and the subsequent annealing at 380 °C in an oxygen-deficient atmosphere.

High energy resolution fluorescence detected X-ray absorption near edge structure (HERFD-XANES) and valence to core X-ray emission spectroscopy (vtc-XES)

To provide further evidence for the oxygen vacancies and to study what electronic structure changes they cause in TiO_2, we performed HERFD-XANES and X-ray emission spectroscopy at beamline ID26 of the European Synchrotron Radiation Facility (ESRF). HERFD-XANES spectra were obtained at the Ti K-edge for bare mp-TiO_2, mp-TiO_2 coated on planar n-Si (planar n-Si/mp-TiO_2), n-Si MWs/mp-TiO_2, and n-Si MWs/mp-TiO_2/α-Fe_2O_3 (Fig. SI 7, ESI†). HERFD-XANES spectra at the Fe K-edge were recorded for bare α-Fe_2O_3, n-Si MWs/α-Fe_2O_3, and n-Si MWs/mp-TiO_2/α-Fe_2O_3 (Fig. SI 8 and SI 9, ESI†). All spectra were normalized to their total area. The spectra were not corrected for over- (or self-) absorption effects that may significantly distort the spectra of the bare oxides. The spectra are thus also presented as first derivatives in order to facilitate comparison.

The Fe K-edge HERFD-XANES taken of all samples are essentially superimposable (Fig. SI 8 and SI 9, ESI†), indicating that neither the deposition of Fe_2O_3 onto mp-TiO_2 nor Si MWs had a significant effect on the electronic structure of α-Fe_2O_3. Similarly, the first derivatives of the Ti K-edge HERFD-XANES spectra of bare mp-TiO_2 and n-Si MWs/mp-TiO_2 are nearly identical (Fig. SI 7, ESI†). This indicates that the contact with the n-Si MWs did not induce significant electronic structural changes in the TiO_2 lattice.

By contrast, the Ti K-edge HERFD-XANES data reveal that the hydrothermal growth of α-Fe_2O_3 nanorods onto mp-TiO_2 strongly influences the electronic structure of mp-TiO_2, as shown in Fig. 6a and b. For Ti, the XANES pre-edge peaks in the energy range of ~4966 to ~4976 eV reflect core electron transition to Ti-3d4p hybridized states, which are highly sensitive to the local geometry of the Ti centers.[59,60] The pre-edge peak A1 corresponds to the transition of a Ti 1s electron into a t_{1g} band-like state. The small low energy shoulder on the A2 peak (A2*) is due to 1s-e_g excitation, while the 1s electron

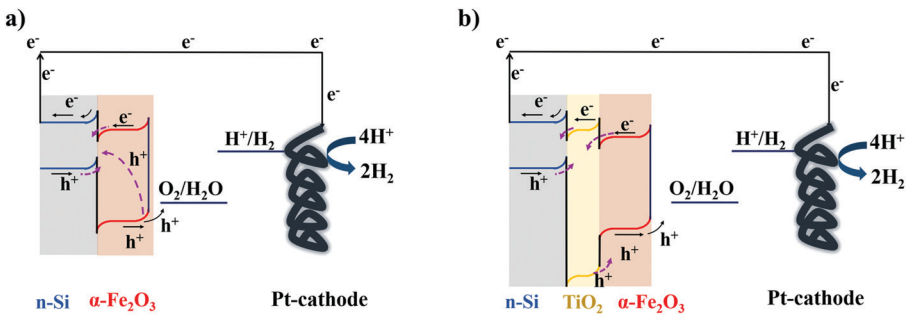

Fig. 5 Schematic band bending diagrams for functionalized n-Si photoanode under an applied anodic bias of 1.5 V. (a) n-Si MWs/α-Fe_2O_3 and (b) n-Si MWs/TiO_2/α-Fe_2O_3 depict the charge carrier transfer under one sun illumination. The possible charge carrier recombination pathways are shown with dashed purple arrows.

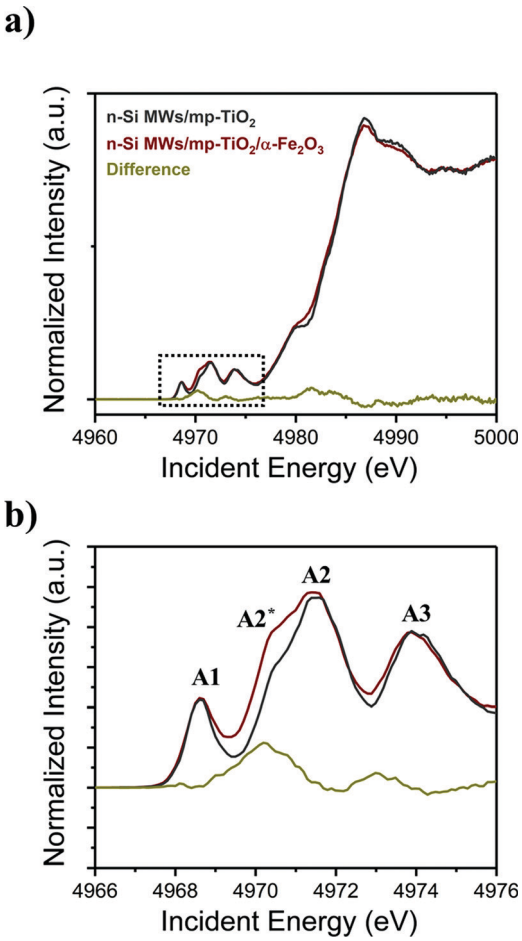

Fig. 6 (a) HERFD-XANES spectra acquired for functionalized n-Si MWs photoanodes at the Ti K-edge, (b) magnified view of the pre-edge region. Additional control spectra are displayed in Fig. SI 7 (ESI†).

excitation to crystal field split d-states on the neighboring Ti atoms results in the main A2 and the A3 peaks.[61,62] The A3 peak corresponds to an e_g band-like state, which is due to pure non-local excitation. The non-local excitations are mediated by oxygen nearest neighbors.[63,64] The surrounding oxygen thus influences all the pre-edge peaks in the Ti K-edge.[59,65–68]

Comparison of the pre-edge features of the n-Si MWs/mp-TiO_2 photoelectrodes with (red line) and without (grey line) α-Fe_2O_3 nanorods (Fig. 6b) reveals that the A2* peak becomes significantly more prominent when α-Fe_2O_3 nanorods are present. At the same time, the other features are unchanged, indicating no significant structural changes. As the A2* peak arises from a 1s–e_g excitation, the presence of a stronger A2* peak in n-Si MWs/mp-TiO_2/α-Fe_2O_3 is attributed to the creation of oxygen vacancies at the mp-TiO_2 and α-Fe_2O_3 interface that leads to a distortion of the local coordination which increases the mixing of metal p and d orbitals.[48] The absence of a shift of the main K-edge shows that the Ti–O distances, on average, do not change,[68,69] indicating that the bulk of the Ti remains in oxidation state Ti^{4+}.

In line with our results, Ghaffari *et al.*[70] reported that the increase in the Ti K-edge A2* pre-edge peak intensities correlates with improved photocatalytic properties of their $SrTi_{(1-\chi)}Fe_\chi O_{(3-\delta)}$ system, which are caused by oxygen vacancies or defects. As the vacancies were created during the hydrothermal growth of α-Fe_2O_3 nanorods and subsequent annealing at 380 °C, we propose that they are restricted to the interface between mp-TiO_2 and α-Fe_2O_3. The band-bending physics presented in Fig. 5b shows that these oxygen vacancies could trap part of the electrons photogenerated in the α-Fe_2O_3 nanorods. This would then effectively inhibit the recombination of charge-carriers in the α-Fe_2O_3 nanorods, leaving the photogenerated holes available for enhanced water oxidation.

To comprehend further the changes in the electronic structure of the mp-TiO_2 interlayer caused by growing Fe_2O_3 nanorods onto it, X-ray emission spectroscopy (XES) was performed at the Ti and Fe K-edges. The Kβ fluorescence lines for Ti are shown in Fig. 7, while the Fe Kβ-XES is displayed in Fig. SI 10 (ESI†). Fig. 7b shows that the 3p to 1s core–shell-to-core–shell ($K\beta_{1,3}$) line of Ti is invariant to the presents of Fe_2O_3 nanorods, and the same is observed for the corresponding Fe signal (Fig. SI 10b, ESI†). As $K\beta_{1,3}$ lines are known to be sensitive to the local spin and thus the oxidation state, the absence of a detectable change indicates that the local distortion of the oxygen environment does not involve redox changes of Ti^{4+} or Fe^{3+}, in line with the observation in the XANES data. The valence-to-core emission lines at higher energies (Fig. 7c and d) arise from metal–ligand mixed orbitals and directly probe the ligand environment. Here we do observe changes for Ti, in agreement with the K absorption pre-edge spectral changes. It is important to note that the maximum amount of TiO_2 that can interact with a ~20 nm diameter α-Fe_2O_3 nanorods is ~20%; for detailed calculation, see the ESI.† The percentage of Ti atoms changing the local coordination as derived from the spectral changes in Fig. 6 is in approximate agreement with the estimated interaction of mp-TiO_2 with α-Fe_2O_3 nanorods. Thus, we suggest that the oxygen vacancies created in mp-TiO_2 are restricted to the interfacial boundary between mp-TiO_2 and the α-Fe_2O_3 nanorods. This suggests that Fe^{3+} ions can stabilize oxygen vacancies at this interface, which in turn prevent electron–hole recombination and thereby enhance the water oxidation activity.[49,50,71–74]

We found that electronic structural changes take place in the mp-TiO_2 when sandwiched between n-Si MW and α-Fe_2O_3, while the Fe-edge hardly changed. This indicates that the improved photocatalysis arises from improved carrier transport within the device rather than a lowered barrier for water splitting at α-Fe_2O_3. This is consistent with our recent finding that p-Si MWs/TiO_2 photocathodes undergo significant changes when decorated with NiO_x or CoO_x.[8] Thus, our study paves the way towards understanding the crucial role of the TiO_2 interlayer by providing X-ray spectroscopic evidence for the stabilization of oxygen vacancies by the application of Fe_2O_3.

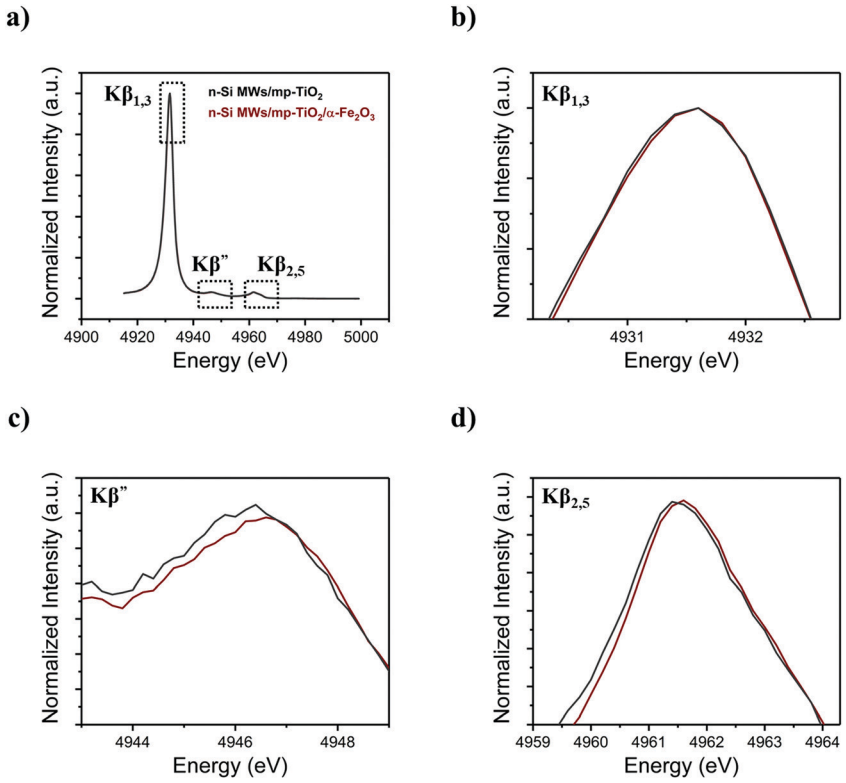

Fig. 7 Ti Kβ XES spectra acquired for functionalized n-Si MWs photoanodes with (a) Kβ main and vtc-XES, (b) $K\beta_{1,3}$, (c) Kβ′ and (d) $K\beta_{2,5}$.

Conclusions

In conclusion, we report here a dual solar photon absorber system comprised of n-Si MWs and α-Fe_2O_3. The n-Si MWs and the α-Fe_2O_3 were connected by a thin mp-TiO_2 layer, which acted as a template for the growth of α-Fe_2O_3 nanorods. In the absence of the mp-TiO_2 interlayer, the overall photo-electrochemical performance of α-Fe_2O_3 functionalized n-Si MWs was significantly reduced. Favorable band bending in the n-Si MWs/mp-TiO_2/α-Fe_2O_3 photoanodes was found to be the critical factor for decreasing the charge recombination and thus increasing the availability of holes for water oxidation. A thorough investigation using X-ray spectroscopy suggests that the hydrothermal growth of α-Fe_2O_3 nanorods on n-Si MWs/mp-TiO_2 with subsequent annealing at 380 °C led to favorable changes in the electronic structure of mp-TiO_2. By contrast, the electronic structure of α-Fe_2O_3 was hardly affected by mp-TiO_2. In summary, the mp-TiO_2 interlayer presented in this study acts (i) as a protective layer for n-Si MWs, (ii) as a template for the uniform and high surface area hydrothermal growth of the α-Fe_2O_3 nanorods, and (iii) in combination with Fe_2O_3, it suppresses charge recombination at the mp-TiO_2/α-Fe_2O_3 interface *via* stabilized oxygen vacancies (electron traps).

We expect that, in the future, this multi-functionality of the TiO_2 interlayer can be utilized in developing further improved photo-electrodes. As exemplified here, the detailed X-ray spectroscopic characterization of the photoelectrodes will be a crucial analytical tool in this process.

Author contribution

A. K., A. A., T. W., P. G., J. M. conceptualize and conceived the project. A. K. prepared all the samples and collected SEM images. A. K. and A. A. performed all the photo-electrochemical experiments. A. K. and A. S. analyzed the GC data. A. K. and P. G. performed a synchrotron experiment and collected HERFD-XANES and XES data. A. K., J. U., P. G. processed and analyzed HERFD-XANES, XES, and XPS data. A. K., and J. U. estimated and compared the fractional contact between mp-TiO_2 and α-Fe_2O_3 nanorods. P. G., and J. M. supervised the research work and discussed the results. A. K., P. G., and J. M. co-wrote the manuscript with important inputs from the co-authors.

Conflicts of interest

The authors declare no competing financial interest.

Acknowledgements

The authors thank Andrey Shchukarev for collecting the XPS data. The SEM images were obtained at the Umeå Core Facility for Electron Microscopy (UCEM). The authors thank European

Synchrotron Radiation Facility for granting beamtime and the ID26 beamline staff for assistance during the experiments. The Knut and Alice Wallenbergs Foundation (Artificial Leaf Project; KAW 2011.0055) provided financial support. T. W. acknowledges support from Vetenskapsrådet (2017-04862), and Energimyndigheten (45419-1).

References

1 M. Grätzel, *Nature*, 2001, **414**, 338.
2 N. S. Lewis, *Science*, 2007, **315**, 798–801.
3 A. Kawde, A. Vats, R. Shende and J. Puszynski, *Nanotechnology*, 2011, **1**, 747–750.
4 A. Fujishima and K. Honda, *Nature*, 1972, **238**, 37.
5 A. Annamalai, A. Subramanian, U. Kang, H. Park, S. H. Choi and J. S. Jang, *J. Phys. Chem. C*, 2015, **119**, 3810–3817.
6 A. Annamalai, P. S. Shinde, A. Subramanian, J. Y. Kim, J. H. Kim, S. H. Choi, J. S. Lee and J. S. Jang, *J. Mater. Chem. A*, 2015, **3**, 5007–5013.
7 R. van de Krol and Y. Liang, *Chimia*, 2013, **67**, 168–171.
8 A. Kawde, A. Annamalai, L. Amidani, M. Boniolo, W. L. Kwong, A. Sellstedt, P. Glatzel, T. Wågberg and J. Messinger, *Sustainable Energy Fuels*, 2018, **2**, 2215–2223.
9 E. L. Warren, H. A. Atwater and N. S. Lewis, *J. Phys. Chem. C*, 2013, **118**, 747–759.
10 A. Kawde, A. Annamalai, A. Sellstedt, P. Glatzel, T. Wågberg and J. Messinger, *Dalton Trans.*, 2019, **48**, 1166–1170.
11 W. L. Kwong, C. C. Lee and J. Messinger, *J. Phys. Chem. C*, 2016, **120**, 10941–10950.
12 J. Luo, L. Steier, M.-K. Son, M. Schreier, M. T. Mayer and M. Grätzel, *Nano Lett.*, 2016, **16**, 1848–1857.
13 W. Niu, T. Moehl, W. Cui, R. Wick-Joliat, L. Zhu and S. D. Tilley, *Adv. Energy Mater.*, 2018, **8**, 1702323.
14 F. Ambrosio, J. Wiktor and A. Pasquarello, *ACS Energy Lett.*, 2018, **3**, 829–834.
15 H. S. Han, S. Shin, D. H. Kim, I. J. Park, J. S. Kim, P.-S. Huang, J.-K. Lee, I. S. Cho and X. Zheng, *Energy Environ. Sci.*, 2018, **11**, 1299–1306.
16 Y. Liang and J. Messinger, *Phys. Chem. Chem. Phys.*, 2014, **16**, 12014–12020.
17 L. Zhang, X. Ye, M. Boloor, A. Poletayev, N. A. Melosh and W. C. Chueh, *Energy Environ. Sci.*, 2016, **9**, 2044–2052.
18 I. Narkeviciute, P. Chakthranont, A. J. Mackus, C. Hahn, B. A. Pinaud, S. F. Bent and T. F. Jaramillo, *Nano Lett.*, 2016, **16**, 7565–7572.
19 B. A. Pinaud, P. C. Vesborg and T. F. Jaramillo, *J. Phys. Chem. C*, 2012, **116**, 15918–15924.
20 Z. Chen, T. F. Jaramillo, T. G. Deutsch, A. Kleiman-Shwarsctein, A. J. Forman, N. Gaillard, R. Garland, K. Takanabe, C. Heske and M. Sunkara, *J. Mater. Res.*, 2010, **25**, 3–16.
21 ASTM International ASTM Standard G173-03 DOI: 10.150/G0173-03R08 (ASTM, 2008); available *via*, www.astm.org.
22 Y. Yu, Z. Zhang, X. Yin, A. Kvit, Q. Liao, Z. Kang, X. Yan, Y. Zhang and X. Wang, *Nat. Energy*, 2017, **2**, 17045.
23 B. Seger, A. B. Laursen, P. C. Vesborg, T. Pedersen, O. Hansen, S. Dahl and I. Chorkendorff, *Angew. Chem., Int. Ed.*, 2012, **51**, 9128–9131.
24 M. J. Kenney, M. Gong, Y. Li, J. Z. Wu, J. Feng, M. Lanza and H. Dai, *Science*, 2013, **342**, 836–840.
25 K. Sun, N. Park, Z. Sun, J. Zhou, J. Wang, X. Pang, S. Shen, S. Y. Noh, Y. Jing and S. Jin, *Energy Environ. Sci.*, 2012, **5**, 7872–7877.
26 S. Hu, M. R. Shaner, J. A. Beardslee, M. Lichterman, B. S. Brunschwig and N. S. Lewis, *Science*, 2014, **344**, 1005–1009.
27 M. R. Shaner, S. Hu, K. Sun and N. S. Lewis, *Energy Environ. Sci.*, 2015, **8**, 203–207.
28 M. F. Lichterman, A. I. Carim, M. T. McDowell, S. Hu, H. B. Gray, B. S. Brunschwig and N. S. Lewis, *Energy Environ. Sci.*, 2014, **7**, 3334–3337.
29 T. Moehl, J. Suh, L. Sévery, R. Wick-Joliat and S. D. Tilley, *ACS Appl. Mater. Interfaces*, 2017, **9**, 43614–43622.
30 W. Cui, W. Niu, R. Wick-Joliat, T. Moehl and S. D. Tilley, *Chem. Sci.*, 2018, **9**, 6062–6067.
31 B. Seger, T. Pedersen, A. B. Laursen, P. C. Vesborg, O. Hansen and I. Chorkendorff, *J. Am. Chem. Soc.*, 2013, **135**, 1057–1064.
32 D. Bae, B. Seger, P. C. Vesborg, O. Hansen and I. Chorkendorff, *Chem. Sci. Rev.*, 2017, **46**, 1933–1954.
33 S. A. Lee, S. Choi, C. Kim, J. W. Yang, S. Y. Kim and H. W. Jang, *ACS Mater. Lett.*, 2019, **2**, 107–126.
34 R. Fan, Z. Mi and M. Shen, *Opt. Express*, 2019, **27**, A51–A80.
35 S. Hu, M. H. Richter, M. F. Lichterman, J. Beardslee, T. Mayer, B. S. Brunschwig and N. S. Lewis, *J. Phys. Chem. C*, 2016, **120**, 3117–3129.
36 P. Wang, X. Wen, R. Amal and Y. H. Ng, *RSC Adv.*, 2015, **5**, 5231–5236.
37 K. Peng, Y. Wu, H. Fang, X. Zhong, Y. Xu and J. Zhu, *Angew. Chem., Int. Ed.*, 2005, **44**, 2737–2742.
38 K. Liu, H. Fu, K. Shi, F. Xiao, L. Jing and B. Xin, *J. Phys. Chem. B*, 2005, **109**, 18719–18722.
39 S. Y. Choi, M. Mamak, N. Coombs, N. Chopra and G. A. Ozin, *Adv. Funct. Mater.*, 2004, **14**, 335–344.
40 L. Vayssieres, N. Beermann, S.-E. Lindquist and A. Hagfeldt, *Chem. Mater.*, 2001, **13**, 233–235.
41 A. Tofanello, S. Shen, F. L. de Souza and L. Vayssieres, *APL Mater.*, 2020, **8**, 040905.
42 G. Ma, T. Hisatomi and K. Domen, *From molecules to materials*, Springer, 2015, pp. 1–56.
43 H. Jung, S. Y. Chae, C. Shin, B. K. Min, O.-S. Joo and Y. J. Hwang, *ACS Appl. Mater. Interfaces*, 2015, **7**, 5788–5796.
44 J. Deng, Q. Zhuo and X. Lv, *J. Electroanal. Chem.*, 2019, **835**, 287–292.
45 M. T. Mayer, C. Du and D. Wang, *J. Am. Chem. Soc.*, 2012, **134**, 12406–12409.
46 X. Qi, G. She, X. Huang, T. Zhang, H. Wang, L. Mu and W. Shi, *Nanoscale*, 2014, **6**, 3182–3189.
47 Z. Zhou, S. Wu, L. Qin, L. Li, L. Li and X. Li, *J. Mater. Chem. A*, 2018, **6**, 15593–15602.
48 Q. Wu, Q. Zheng and R. van de Krol, *J. Phys. Chem. C*, 2012, **116**, 7219–7226.

49 J. Moser, M. Grätzel and R. Gallay, *Helv. Chim. Acta*, 1987, **70**, 1596–1604.
50 W. Choi, A. Termin and M. R. Hoffmann, *J. Phys. Chem.*, 2002, **98**, 13669–13679.
51 S. Jayashree and M. Ashokkumar, *Catalysts*, 2018, **8**, 601.
52 M. K. Nowotny, L. R. Sheppard, T. Bak and J. Nowotny, *J. Phys. Chem. C*, 2008, **112**, 5275–5300.
53 X. Pan, M.-Q. Yang, X. Fu, N. Zhang and Y.-J. Xu, *Nanoscale*, 2013, **5**, 3601–3614.
54 R. F. Howe and M. Gratzel, *J. Phys. Chem.*, 1985, **89**, 4495–4499.
55 K. He, C. Zhao, G. Zhao and G. Han, *J. Sol-Gel Sci. Technol.*, 2015, **75**, 557–563.
56 P. Hartmann, D.-K. Lee, B. M. Smarsly and J. Janek, *ACS Nano*, 2010, **4**, 3147–3154.
57 M. Zukalova, A. Zukal, L. Kavan, M. K. Nazeeruddin, P. Liska and M. Grätzel, *Nano Lett.*, 2005, **5**, 1789–1792.
58 L. Kavan, J. Rathouský, M. Grätzel, V. Shklover and A. Zukal, *Microporous Mesoporous Mater.*, 2001, **44**, 653–659.
59 P. C. Angelome, L. Andrini, M. E. Calvo, F. G. Requejo, S. A. Bilmes and G. J. Soler-Illia, *J. Phys. Chem. C*, 2007, **111**, 10886–10893.
60 D. Cabaret, Y. Joly, H. Renevier and C. Natoli, *J. Synchrotron Radiat.*, 1999, **6**, 258–260.
61 Y. Joly, D. Cabaret, H. Renevier and C. R. Natoli, *Phys. Rev. Lett.*, 1999, **82**, 2398.
62 J. Szlachetko, K. Michalow-Mauke, M. Nachtegaal and J. Sá, *J. Chem. Sci.*, 2014, **126**, 511–515.
63 P. Glatzel, L. Jacquamet, U. Bergmann, F. M. de Groot and S. P. Cramer, *Inorg. Chem.*, 2002, **41**, 3121–3127.
64 P. Glatzel, A. Mirone, S. G. Eeckhout, M. Sikora and G. Giuli, *Phys. Rev. B: Condens. Matter Mater. Phys.*, 2008, **77**, 115133.
65 V. Luca, S. Djajanti and R. F. Howe, *J. Phys. Chem. B*, 1998, **102**, 10650–10657.
66 R. Brydson, H. Sauer, W. Engel, J. Thomass, E. Zeitler, N. Kosugi and H. Kuroda, *J. Phys.: Condens. Matter*, 1989, **1**, 797.
67 L. Amidani, A. Naldoni, M. Malvestuto, M. Marelli, P. Glatzel, V. Dal Santo and F. Boscherini, *Angew. Chem., Int. Ed.*, 2015, **54**, 5413–5416.
68 P. Glatzel and U. Bergmann, *Coord. Chem. Rev.*, 2005, **249**, 65–95.
69 P. Glatzel, T.-C. Weng, K. Kvashnina, J. Swarbrick, M. Sikora, E. Gallo, N. Smolentsev and R. A. Mori, *J. Electron Spectrosc. Relat. Phenom.*, 2013, **188**, 17–25.
70 M. Ghaffari, T. Liu, H. Huang, O. K. Tan and M. Shannon, *Mater. Chem. Phys.*, 2012, **136**, 347–357.
71 G. Glaspell and A. Manivannan, *J. Cluster Sci.*, 2005, **16**, 501–513.
72 M. Zhou, J. Yu, B. Cheng and H. Yu, *Mater. Chem. Phys.*, 2005, **93**, 159–163.
73 J. Soria, J. Conesa, V. Augugliaro, L. Palmisano, M. Schiavello and A. Sclafani, *J. Phys. Chem.*, 1991, **95**, 274–282.
74 J. C. Yu, W. Ho, J. Lin, H. Yip and P. K. Wong, *Environ. Sci. Technol.*, 2003, **37**, 2296–2301.